Hindawi Publishing Corporation
EURASIP Journal on Applied Signal Processing
Volume 2006, Article ID 74838, Pages 1–16
DOI 10.1155/ASP/2006/74838

Knowledge-Aided STAP Processing for Ground Moving Target Indication Radar Using Multilook Data

Douglas Page and Gregory Owirka

BAE Systems Advanced Information Technologies, 6 New England Executive Park, Burlington, MA 01803, USA

Received 7 November 2004; Revised 16 February 2005; Accepted 8 March 2005

Knowledge-aided space-time adaptive processing (KASTAP) using multiple coherent processing interval (CPI) radar data is described. The approach is based on forming earth-based clutter reflectivity maps to provide improved knowledge of clutter statistics in nonhomogeneous terrain environments. The maps are utilized to calculate predicted clutter covariance matrices as a function of range. Using a data set provided under the DARPA knowledge-aided sensor signal processing and expert reasoning (KASSPER) Program, predicted distributed clutter statistics are compared to measured statistics to verify the accuracy of the approach. Robust STAP weight vectors are calculated using a technique that combines covariance tapering, adaptive estimation of gain and phase corrections, knowledge-aided prewhitening, and eigenvalue rescaling. Techniques to suppress large discrete returns, expected in urban areas, are also described. Several performance metrics are presented, including signal-to-interference-plus-noise ratio (SINR) loss, target detections and false alarms, receiver operating characteristic (ROC) curves, and tracking performance. The results show more than an order of magnitude reduction in false alarm density when compared to standard STAP processing.

1. INTRODUCTION

The lack of training data in nonhomogeneous clutter environments can cause severe degradation in the performance of space-timeadaptive processing (STAP) algorithms (see [1, 2] and references therein). Surveillance radars typically perform STAP processing [3] on a limited number of pulses of data, which are referred to as a coherent processing interval (CPI). Each CPI is divided into a number of time samples which correspond to the radar range gates. In each range gate, the return signal in each antenna channel and on each pulse in the CPI is digitized into in-phase and quadrature components. The radar returns can thus be represented as complex numbers, whose real parts are the corresponding in-phase components, and whose imaginary parts are the quadrature components. Thus, in each range gate the returns from each channel and pulse can be represented as an NM by 1 complex column vector, where N is the number of antenna channels and M the number of pulses per CPI. Covariance estimation for STAP is usually performed by averaging the outer products of these return vectors with themselves over a number of training range gates from a single CPI. As was shown by Reed et al. [4], this is a maximum likelihood estimate of the clutter covariance matrix, assuming zero-mean complex Gaussian and homogeneous (i.e., range-independent) statistics.

Due to varying terrain conditions, the covariance estimation just described may result in poor estimates, due to an inadequate amount of training data matching the range gate under test. Two possible consequences of this are undernulling or overnulling of clutter. Undernulling may occur if the test range gate contains strong clutter due to, say, steeply sloped terrain, while the training window surrounding the test cell contains less severe clutter. This may lead to an excessive number of false alarms or, if the threshold is increased to reduce false alarms, loss of target detections. Overnulling of clutter may occur when the training window contains steeply sloped terrain or windblown clutter that is not present in the target range cell. Overnulling leads to the loss of target detections.

The motivation for the study described here is the fact that in surveillance radar scenarios, a given area on the ground may contribute to clutter returns over *multiple* CPIs. The data cubes from these CPIs contain potential training data for estimating covariance matrices which, if exploited properly, can reduce the degradation caused by range-varying terrain. Due to the fact that the platform geometry is changing from CPI to CPI, however, the space-time response

of clutter scattered from a given point on the ground will also be changing. Moreover, the area of intersection between the radar resolution cells and the earth's surface will also be changing with platform geometry. Thus, simply averaging outer products of complex returns from additional CPI data cubes to augment standard covariance estimation is not effective (and may in fact cause STAP performance to degrade rather than improve).

Additionally, in actual ground moving target indication (GMTI) surveillance systems there are a number of real-world effects that can degrade the performance of knowledge-aided STAP techniques. Unknown antenna pattern mismatch and internal clutter motion can cause model errors and undernulled residual clutter. High ground target densities produce target contamination of the STAP training data, thus producing filter nulls at the locations of the desired targets. Returns from large discretes, such as buildings in urban areas, are spatially localized and can be much larger than the returns from distributed clutter. These returns can cause numerous false alarms that are spread over a wide area due to sidelobe effects. Effective suppression of such discrete returns may require specialized techniques in addition to those used for distributed nohomogeneous clutter.

In order to exploit multilook radar data, an effective knowledge-aided STAP approach must be able to extract information from each CPI on clutter statistics, correct for CPI-to-CPI differences in the statistics, and calculate STAP weight vectors that are robust under real-world GMTI conditions. Our approach to accomplish these objectives combines a number of different techniques, which are listed below:

(1) formation of earth-referenced clutter reflectivity maps using multiple CPIs,
(2) covariance tapering to model internal clutter motion [5],
(3) extended-factored (or "adjacent bin") post-Doppler processing [6],
(4) adaptive estimation and correction for channel and Doppler-dependent gain and phase errors,
(5) knowledge-aided prewhitening using the colored loading technique of [7, 8],
(6) eigenvalue rescaling of the knowledge-aided covariance matrix,
(7) masking of STAP training data using a two-pass procedure to reduce the effects of targets on the covariance estimates,
(8) specialized processing to detect and remove returns from large discretes such as buildings.

We have listed where appropriate references by other authors that are employed in each technique. Covariance tapering is described in [5] and is applied to the covariance matrices derived from the clutter reflectivity map. This models the effects of internal clutter motion (ICM), which is an important real-world phenomenon. We used post-Doppler STAP degrees of freedom known as extended-factored or adjacent-bin post-Doppler STAP [6]. The knowledge-aided prewhitening algorithm developed by Bergin et al. [7, 8] is also an important part of the approach. However, we have also found the nonreferenced algorithm components listed above that we developed (i.e., techniques (1), (4), (6), (7), (8)) to improve STAP performance significantly. In addition, we consider a performance metric not normally shown in the literature. In addition to the usual signal-to-interference-plus-noise ratio (SINR) loss metric, we also study the residual clutter-to-noise ratio (CNR) after STAP processing. The latter is especially important, as it determines the number of false alarms that will be observed after constant false alarm rate (CFAR) processing is performed. To further quantify the benefits of our approach we also show receiver operating characteristic (ROC) curves of detection probability versus false alarm density.

An outline of the paper is as follows. We describe in Section 2 techniques (1)–(6) in detail. In Section 3, we consider target contamination effects (technique (7)) and show the results of processing the KASSPER Data Set 2 [9]. The results obtained indicate that significant improvements in STAP performance may indeed be achieved by incorporating multiple CPI data cubes into knowledge-aided STAP processing using the approach we describe. In Section 4, we show the degrading effects of strong clutter discretes on GMTI KASTAP performance. We describe additional KASTAP techniques for suppressing these discretes and show results that indicate these techniques are effective in eliminating the degradation caused by large discretes. Finally, Section 5 summarizes our results.

2. ALGORITHM DESCRIPTION FOR DISTRIBUTED CLUTTER MITIGATION

2.1. Formation of clutter reflectivity maps

The first aspect of our KASTAP approach using multilook radar data is to form earth-referenced clutter reflectivity maps. The goal of this step is to extract estimates of clutter return strength as a function of spatial location on each CPI and to incorporate these estimates into a clutter map defined in a single common coordinate system. This compensates for the differences in the radar coordinate systems on each CPI and allows information on clutter statistics derived from multiple CPI looks to be utilized in determining the STAP filter weights on subsequent CPIs. By incorporating estimates from multiple CPIs over an extended time period, the effects of random estimation errors and target contamination effects on the clutter return estimates are reduced through the averaging process.

As illustrated in Figure 1, there are four basic steps involved in forming a clutter reflectivity map from multiple CPI data cubes. These steps are described individually below.

2.1.1. Definition of clutter scatterers

The first step in extracting information on clutter statistics on a given CPI is to define a clutter environment model. The model we developed was tailored to distributed clutter returns from terrain over an extended area on the earth. The effects of localized discrete returns, such as those due to

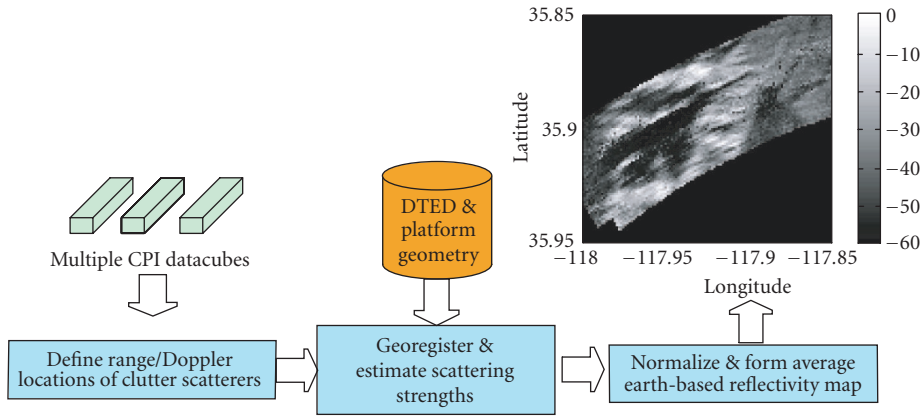

Figure 1: Illustration of procedure for forming an earth-based clutter reflectivity map.

Table 1: KASSPER Data Set 2 parameters [9].

Quantity	Value
Radar frequency	10 GHz
Radar bandwidth	10 MHz
Peak power	10 kW
System losses	7 dB
Antenna size	1.43 m (horizontal) by .285 m (vertical)
Transmit antenna pattern	Spoiled to 10-degree beamwidth
Receive antenna configuration	12 nonoverlapping subarrays, spaced by 4 wavelengths per subarray
Number of pulses per CPI	38
Number of CPIs per dwell	3 with PRFs of 2081, 1800, and 1518 Hz
Time separation of dwells	10 s
Number of dwells in scenario	30
Platform motion	150 m/s, heading west
Crab angle	3°
Standoff range to targets	Approximately 45 km
Target clusters	3 clusters, 60 vehicles each
Background traffic	1000 vehicles
Target motion	Move along roads, speed 2–25 m/s depending on road type, decelerate when approaching intersections
Earth model	Spherical, radius 6 378 388 m, modulated by DTED

large buildings in urban areas, will be considered separately in Section 4. To motivate the distributed clutter environment model, we first discuss the characteristics of the KASSPER Data Set 2 that was processed. The parameters for this data set are given in Table 1.

The antenna elements of the KASSPER Data Set are formed using 12 nonoverlapped subarrays spaced by 4 wavelengths per subarray. The subarrays are presteered to a particular direction on each CPI. The azimuth and elevation angle of this presteering direction are supplied along with the data cube for each CPI. Each CPI contains 38 pulses, and a dwell consisting of three consecutive CPIs at different pulse repetition frequencies (PRFs) occurs every 10 seconds. During this time interval, the platform moves 1.5 km. This is significant relative to the 40 km standoff range to the targets, as small CPI-to-CPI changes in aspect angle can produce large changes in the space-time response of clutter scatterers.

With the parameters shown in Table 1, a Doppler resolution cell located broadside to the platform spans approximately 0.3 degrees in azimuth. This is a factor of 4 finer than the antenna beamwidth of 1.2 degrees. Thus, the Doppler filter spacing is about 1/4 of the antenna beamwidth (as one moves off broadside, the Doppler filter width and antenna beamwidth are both inversely proportional to the cosine of the azimuth steering angle). Consequently, modeling the clutter environment as a set of point scatterers spaced apart by no more than one Doppler filter should result in oversampling of the radar azimuth resolution. The bandwidth of the system shown in Table 1 leads to a range resolution of 15 m, which is much smaller than the size of the antenna beams or Doppler filters on the ground. Thus, one scatterer per range cell should suffice to give accurate clutter statistics.

The Doppler extent of the scatterers assumed in each range gate is limited by the fact that the spatial response across the antenna subarrays has grating lobes due to the 4 wavelength spacing. If the extent is selected to be too large, the space-time response of two different clutter scatterers can become nearly the same due to the simultaneous presence of a temporal (Doppler) and spatial ambiguity. This would prevent accurate estimation of the relative scattering strengths of the two scatterers. In order to avoid this problem while simulating the effects of sidelobe clutter, scatterers were selected to span the main Doppler ambiguity plus 30% of each of the Doppler ambiguities on either side of the main ambiguity.

2.1.2. *Georegistration of clutter scatterers*

The clutter environment model described above is tied to a radar coordinate system, which is the natural coordinate system to use when estimating clutter parameters on a given CPI look. As mentioned above, in order to combine clutter

estimates from multiple CPIs, we define a common earth-based coordinate system. The process by which the location of the model clutter scatterers from a given CPI on the earth is determined is referred to as georegistration. The ground location of a clutter scatterer is defined by the intersection of three surfaces:

(a) a range sphere centered on the platform location, having a radius equal to the slant range R_s of the scatterer,
(b) a cone about the platform velocity vector, corresponding to the Doppler frequency of the scatterer. Neglecting internal clutter motion, the cosine of the cone angle relative to the platform velocity vector is given by

$$\cos\theta_c = \frac{\lambda f_{\text{dop}}}{2V_p}, \tag{1}$$

where λ is the radar wavelength, f_{dop} the scatterer Doppler frequency, and V_p the radar platform speed,
(c) the earth's surface. This is defined by digital terrain elevation data (DTED).

The height of the earth's surface at a scatterer location depends on its latitude and longitude, and these are unknown. An iterative approach using an initial estimate of the terrain height h above the reference spherical earth model of radius R_e was employed. Let the unknown position of the scatterer in earth-centered coordinates be denoted by $\mathbf{r}_{\text{sc}}$. The platform position vector is known and is denoted by $\mathbf{r}_p$. The scatterer position is then determined by solving the following three equations:

$$\begin{aligned} \left|\mathbf{r}_{\text{sc}} - \mathbf{r}_p\right|^2 &= {R_s}^2 \quad \text{(range sphere)},\\ \left(\mathbf{r}_{\text{sc}} - \mathbf{r}_p\right) \bullet \mathbf{v}_p &= R_s \cdot V_p \cdot \cos\theta_c \quad \text{(Doppler cone)},\\ \left|\mathbf{r}_{\text{sc}}\right|^2 &= \left(R_e + h\right)^2 \quad \text{(earth sphere)}. \end{aligned} \tag{2}$$

The above equations constitute a set of three equations and three unknowns, which are the three components of the scatterer position vector $\mathbf{r}_{\text{sc}}$. To refine the value of h, the earth-centered position vector $\mathbf{r}_{\text{sc}}$ is converted to latitude and longitude using spherical earth geometry. The new terrain height is then obtained by accessing the DTED database at this location. Several iterations of this procedure were employed to reduce the geolocation error to a small fraction of a resolution cell. For the study described in this paper, a level 1 database indexed by latitude and longitude having a posting of 90 m was employed (note from Table 1 that in the KASSPER Data Set these height variations occur on a reference spherical rather than ellipsoidal earth).

2.1.3. Estimation of scatterer strengths

Once the scatterer locations on the ground are determined, their contributions to the received radar amplitudes must be estimated. This first requires defining the space-time steering vectors to each scatterer. Assuming identical antenna channels, the elements of a steering vector are a known function of the look direction to the scatterer and its Doppler frequency. The magnitude of the steering vector elements is also scaled by the overall (channel-independent) subarray azimuth antenna gain on the scatterer. This is done in order to correct for known CPI-to-CPI changes in this antenna pattern, and it is important for clutter scatterers that are near the edge of the mainlobe region of the subarray pattern. As the platform geometry changes, such scatterers can move into the mainlobe and produce a significantly larger return, or move into the sidelobe region and produce a weaker return. (We only assume that the overall pattern is known and is the same for all the antenna channels; to account for channel mismatch we have an adaptive procedure that will be described in Section 2.3.3.)

Let the steering vector to the scatterer i in a given range gate of a given data cube be denoted by $\mathbf{s}_i$. Also let $\mathbf{x}$ be the measured data vector in the range gate. We desire an approximation to $\mathbf{x}$ in the form

$$\mathbf{x} = \sum_i \alpha_i \cdot \mathbf{s}_i. \tag{3}$$

The complex return strengths α_i are selected in order to minimize the squared error

$$\varepsilon = \left|\mathbf{x} - \sum_i \alpha_i \cdot \mathbf{s}_i\right|^2. \tag{4}$$

The solution of this problem can be shown to be

$$\alpha_i = \sum_j \left[\mathbf{S}^{-1}\right]_{ij} \cdot {\mathbf{s}_j}^H \mathbf{x}, \quad [\mathbf{S}]_{ij} \equiv {\mathbf{s}_i}^H \mathbf{s}_j. \tag{5}$$

In general, the matrix $\mathbf{S}$ will not be diagonal, due to the fact that the steering vectors will not be orthogonal. This is true even if the scatterer spacing is selected to be one Doppler filter, due to the fact that multiple Doppler ambiguities are modeled. The complex numbers α_i represent the return strengths and phases of the scatterers in a given range gate of a given data cube. Each of the scatterers represents clutter in one range-Doppler cell, which in turn corresponds to a particular area on the ground. The procedure described here is repeated for all the processed range gates in each of the CPI data cubes used to form a clutter reflectivity map.

2.1.4. Normalization of clutter reflectivity

Since the complex clutter estimates described in Section 2.1.3 are derived from measured data, they implicitly include all the effects of parameters appearing in the radar range equation (i.e., transmit antenna patterns, clutter radar cross section, etc.). The cell areas of range-Doppler resolution cells on the ground are different on each CPI, due to the different pulse repetition frequencies (PRFs), as well as the changing geometry as the platform moves. Because the areas are changing from CPI to CPI, it is important to build the clutter reflectivity map using reflectivity, which normalizes the clutter return power by the cell area. Define $\Delta\mathbf{r}_{\text{rng}}{}^{(i)}$ as the vector on the ground spanning the range dimension of scatterer i, and $\Delta\mathbf{r}_{\text{dop}}{}^{(i)}$ as the vector spanning the Doppler dimension.

The area of the corresponding ground cell is then given by

$$A_i = \left| \Delta \mathbf{r}_{\text{rng}}{}^{(i)} \times \Delta \mathbf{r}_{\text{dop}}{}^{(i)} \right|. \quad (6)$$

The clutter reflectivity of the scatterer is then defined as the estimated clutter power $|\alpha_i|^2$ divided by the area on the ground A_i represented by that scatterer.

2.1.5. Formation of clutter reflectivity maps

The reflectivity maps are built by first determining, for each cell of the map, the range and Doppler indices of the clutter scatterer that encompasses the center of the cell on each CPI. This is accomplished using a straightforward conversion from earth-centered coordinates to radar-centered coordinates. The clutter reflectivity of the cell is then calculated by averaging the estimated reflectivities of the corresponding scatterers over many CPIs. To improve the fidelity of the reflectivity map, reflectivity estimates from the current CPI are incorporated adaptively. It is important to include current-CPI data, since as the platform moves new areas on the ground may contribute significantly to the clutter interference. Additionally, large changes in clutter reflectivity will occur when a ground patch first becomes visible to the radar (producing an increase) or shadowed from the radar by terrain (producing a large decrease in reflectivity). To improve the clutter reflectivity estimates under these conditions, a metric was formulated to detect such changes.

Assume that we have individual clutter reflectivity estimates in a given cell of a ground-based reflectivity map on L past CPIs. These estimates are denoted as r_l, $l = 1, 2, \ldots, L$. We also have a reflectivity estimate r_{L+1} on the current CPI. We assume that each r_l is a random variable with an exponential probability distribution. This is justified by the fact that these estimates are derived as thesquared magnitude of a linear combination of complex Gaussian random variables. To detect reflectivity changes, we define two hypotheses:

$H_0 : r_{L+1}$ has the same mean as $r_{1,2,\ldots,L}$,
$H_1 : r_{L+1}$ has a different mean than $r_{1,2,\ldots,L}$.

The generalized likelihood ratio test (GLRT) for deciding between the two hypotheses (see [10] for a good description of this technique) can be easily shown to have the form

$$(L+1) \cdot \ln \frac{\sum_{l=1}^{L+1} r_l}{L+1} - L \cdot \ln \frac{\sum_{l=1}^{L} r_l}{L} - \ln r_{L+1} > T_G. \quad (7)$$

Here, T_G is the GLRT threshold setting. Normally, the reflectivity map cell value is set equal to the average $\sum_{l=1}^{L+1} r_l/(L+1)$ of the estimated reflectivities over all the CPIs processed. When the GLRT threshold is exceeded, however, the map reflectivity is set equal to the current-CPI estimate r_{L+1}. In this manner, the reflectivity map responds more rapidly as a function of time (CPI) to rapid changes in clutter return strength. A similar approach has been used in [11] to perform SAR change detection.

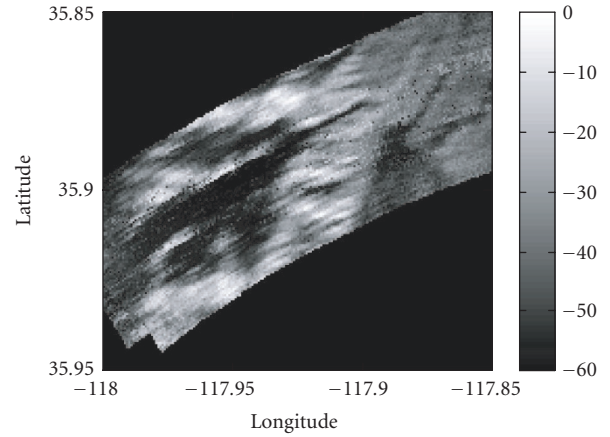

Figure 2: Clutter reflectivity map formed from multiple CPIs of the KASSPER Data Set 2.

Figure 2 shows a clutter reflectivity map that was calculated using CPI #s 17–22 of the KASSPER Data Set 2, with adaptive GLRT processing on CPI #22. The resolution of the map was selected as 25 m, which is slightly larger than the 15 m range resolution. The boundaries of the map correspond to the range limits processed on each CPI. The reflectivity map is seen to predict regions of very strong clutter, which are produced by steeply sloped terrain. In addition there are areas where the reflectivity is much weaker, which includes regions that are shadowed from the radar (i.e., not visible). The knowledge gained from the reflectivity map allows these areas to be identified. The STAP processor can incorporate this knowledge into the adaptive weight vector and reduce the magnitude of over-/undernulling that occurs with standard range-averaged covariance estimation.

2.2. Prediction of current-CPI statistics

In order to be useful in improving STAP detection of slowly moving ground targets, the multi-CPI clutter reflectivity map described above must be employed to calculate clutter statistics for the CPI under test. The procedure used here is to define a grid of model clutter scatterers in each range gate of the data cube, as described in Section 2.1.1. The extent and spacing used for prediction of the statistics can be different than that used for estimation of clutter reflectivity. For the results shown below, scatterers spanning three Doppler ambiguities about the look direction were defined (recall that for estimation, only 1.6 ambiguities were modeled). To reduce interpolation errors, the Doppler spacing of the scatterers was taken to be half a Doppler filter rather than one filter.

Once the scatterer range and Doppler locations used for prediction of current-CPI clutter statistics are defined, registration to geodetic coordinates is performed as described in Section 2.1.2. The steering vectors and cell areas of each scatterer are then calculated as specified in Sections 2.1.3 and 2.1.4. The reflectivity of a particular scatterer on the current-CPI data cube is next determined by using its calculated latitude and longitude and indexing into the clutter reflectivity

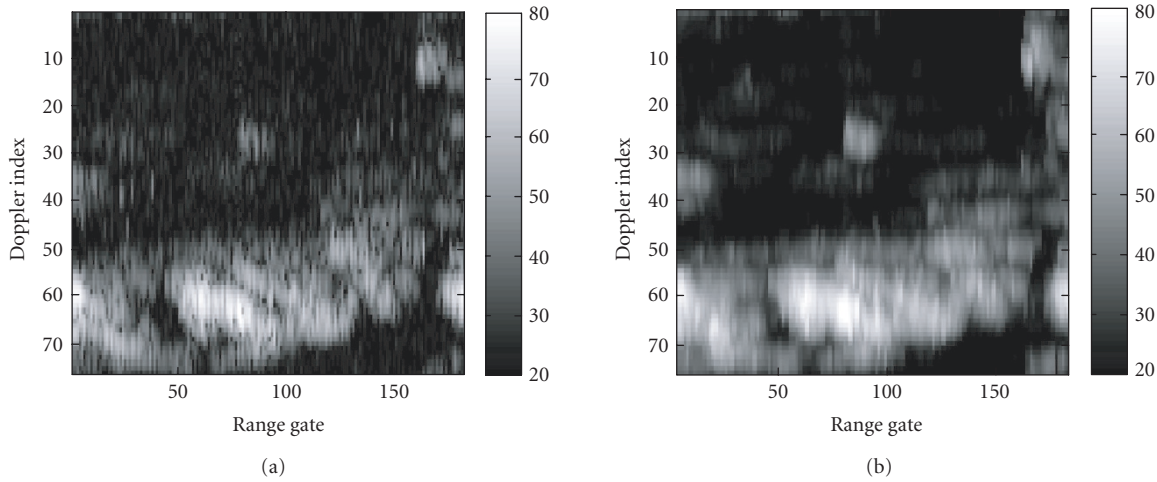

Figure 3: Comparison of (a) measured range-Doppler spectrum for CPI #22 with (b) prediction of clutter reflectivity map.

map. To obtain the estimated power p_i of scatterer i, the reflectivity is multiplied by its cell area A_i. The overall antenna subarray azimuth gain is then applied, which corrects for the changing power of scatterers that may have been in the mainlobe on previous CPIs but have moved into the antenna sidelobes on the current CPI (or vice versa). A covariance matrix for each range gate is then calculated by summing the individual contributions of the scatterers in the range gate:

$$\mathbf{Q}_{\text{calc}} = \sum_i p_i \cdot \mathbf{s}_i \mathbf{s}_i^H. \tag{8}$$

(Note that we use the symbol $\mathbf{Q}$ to denote a full-degree-of-freedom (DOF) covariance matrix across all the antenna elements and pulses. In Section 2.3.2 we will use the symbol $\mathbf{R}$ to denote a reduced-DOF post-Doppler covariance matrix for a given target Doppler index. The reduced DOF set will consist of all antenna elements but a limited number of adjacent Doppler filters surrounding the target filter. If we restrict attention to the center adjacent filter only (i.e., the target filter), the resulting N-by-N spatial covariance matrix will be denoted by the symbol $\mathbf{U}$. To denote the elements of a covariance matrix we use the lower case, nonbold symbols $q_{i,j}$, $r_{i,j}$, $u_{i,j}$ for the full DOF, post-Doppler, and spatial covariance matrices, resp., where i is a row index and j a column index.)

To test the accuracy of the algorithm, a plot of the mean power in each range gate and Doppler filter was calculated. This was done by employing a single spatial weight vector corresponding to the radar look direction and a bank of temporal weight vectors corresponding to a temporal FFT across the CPI. Chebychev weighting (60 dB sidelobes) was applied across the pulses prior to applying the weight vectors in order to reduce the effects of Doppler sidelobes. Figure 3 compares the measured range/Doppler spectrum for CPI #22 with the mean spectrum corresponding to the covariance matrices calculated using the reflectivity map shown in Figure 2.

The clutter in Figure 3 is somewhat confined in Doppler (vertical dimension). This is due to the Doppler extent of the area covered by the antenna beamwidth. The total Doppler extent of the plots is equal to the pulse repetition frequency (equal to 2081.3 Hz for CPI #22). The Doppler interval is oversampled so that the number of Doppler frequencies at which the spectrum is evaluated is equal to two times the number of pulses in the CPI. Note the strong range variation of the clutter (the range extent of the plots is 2.7 km). This is due to the occurrence of varying terrain slopes and shadowing.

Observe that the clutter location in Doppler and its variation with range is correctly predicted, showing that the registration procedure was effective. The returns in the middle of the plots are due to near-sidelobe clutter and are also correctly predicted. The clutter predictions can be expected to produce significant improvements over standard STAP training, which essentially averages the features over the entire range interval.

2.3. STAP weight vector calculation

The approach taken to compute robust STAP weight vectors has several aspects which we now describe.

2.3.1. Covariance tapering

To account for internal clutter motion, the calculated covariance matrices shown in (8) are modified before Doppler processing. Reference [5] shows that the effect of internal clutter motion (ICM) on the covariance matrix is to taper the elements of that matrix. To model a two-sided exponential velocity distribution, a tapering function with a Lorentzian shape is applied to the elements of the covariance matrices calculated from the reflectivity map

$$q_{n+(m-1)\cdot N,n'+(m'-1)\cdot N} \longrightarrow q_{n+(m-1)\cdot N,n'+(m'-1)\cdot N} \cdot \frac{1}{1+\gamma|m-m'|^2}. \tag{9}$$

Note that the row index is defined so that as one moves down

the row, the spatial DOF index (n) is changing more rapidly than the temporal DOF index (m). Similarly, as one moves across a column, the spatial DOF index n' is changing more rapidly than the temporal DOF index m'. The total number of spatial elements is equal to the number of antenna channels N, the number of temporal DOFs is equal to the number of pulses M, and the number of rows or columns is NM.

For the results shown in the next section, the constant γ was selected to correspond to a 0.17 m/s standard deviation of the distribution of clutter internal velocity. This value was selected empirically based upon observations of the data correlation characteristics.

2.3.2. Post-Doppler processing

Once the covariance tapers are applied to the calculated covariance matrices, Doppler preprocessing of the covariance matrices is next performed. To obtain the results shown in the next section, extended-factored [6] (also known as "adjacent-bin" or "multi-bin") post-Doppler processing was implemented in order to reduce the number of adaptive degrees of freedom and required training window sizes. This algorithm calculates a separate STAP weight vector in each Doppler filter, allowing tailoring the adaptive filter to the clutter present in each Doppler filter. This is advantageous when the clutter is strongly varying with Doppler (as was seen in Figure 3). The Doppler preprocessing transformation for a given Doppler filter index i_{dop} is described by a matrix $\mathbf{D}(i_{\text{dop}})$. This matrix has dimensions F_{adj} by M, where F_{adj} is the number of adjacent filters forming the temporal degrees of freedom for target Doppler filter i_{dop}, and M is the number of pulses in the CPI. The elements of $\mathbf{D}(i_{\text{dop}})$ are denoted by $d_{f,m}(i_{\text{dop}})$, where f is the adjacent filter row index and m the pulse column index.

The elements of a reduced-DOF post-Doppler data vector $\mathbf{y}(k, i_{\text{dop}})$ in range gate k and Doppler filter i_{dop} are obtained from those of the full-DOF data vector $\mathbf{x}(k)$ in the range gate using the equation

$$y(k, i_{\text{dop}})_{n+(f-1)\cdot N} = \sum_{m=1}^{M} d_{f,m}(i_{\text{dop}}) \cdot x(k)_{n+(m-1)\cdot N}, \quad n = 1, 2, \ldots, N,\ f = 1, 2, \ldots, F_{\text{adj}}. \tag{10}$$

For the reduced-DOF data vector, the row indices are again defined so that as one moves down a row, the spatial DOF (n) *is* changing more rapidly than the temporal DOF (f). No spatial DOF reduction has been performed, so the spatial DOFs consist of the $N = 12$ antenna subarrays. We selected $F_{\text{adj}} = 3$ temporal DOFs, corresponding to 3 adjacent Doppler filters surrounding the target Doppler filter (or filter under test).

Correspondingly, the elements of a reduced-DOF covariance matrix $\mathbf{R}(k, i_{\text{dop}})$ in the range gate k and the target Doppler filter i_{dop} are given in terms of the elements $q(k)_{n+(m-1)\cdot N, n'+(m'-1)\cdot N}$ of the full-DOF covariance matrix $\mathbf{Q}(k)$ as

$$r(k, i_{\text{dop}})_{n+(f-1)\cdot N, n'+(f'-1)\cdot N} = \sum_{m=1}^{M} \sum_{m'=1}^{M} d_{f,m}(i_{\text{dop}}) \cdot q(k)_{n+(m-1)\cdot N, n'+(m'-1)\cdot N} \cdot d_{f',m'}(i_{\text{dop}})^*, \quad n = 1, 2, \ldots, N,\ n' = 1, 2, \ldots, N,\ f = 1, 2, \ldots, F_{\text{adj}},\ f' = 1, 2, \ldots, F_{\text{adj}}. \tag{11}$$

2.3.3. Adaptive correction for channel mismatch

To compensate for angle- and channel-dependent antenna pattern mismatch, an adaptive estimation of complex correction terms is next performed in each Doppler filter. This is accomplished using a linearized maximum likelihood method to estimate channel-dependent gain and phase error terms. In each Doppler filter, a spatial N-by-N covariance matrix $\mathbf{U}_{\text{calc}}$ is first obtained by extracting the spatial covariance corresponding to the center adjacent filter (f_c) of the reduced-DOF post-Doppler covariance matrix $\mathbf{R}_{\text{calc}}$ calculated from the reflectivity map. The elements of the spatial covariance are given in terms of those of the reduced-DOF post-Doppler covariance as

$$u_{\text{calc}}(k, i_{\text{dop}})_{n,n'} = r_{\text{calc}}(k, i_{\text{dop}})_{n+(f_c-1)\cdot N, n'+(f_c-1)\cdot N}, \quad n, n' = 1, 2, \ldots, N. \tag{12}$$

Phase error terms on each element are first estimated using a maximum likelihood criterion. The effect of the phase errors on the spatial covariance is to produce a corrected covariance $\tilde{\mathbf{U}}_{\text{calc}}(k, i_{\text{dop}})$, whose elements are given by the following equation:

$$\tilde{u}_{\text{calc}}(k, i_{\text{dop}})_{n,n'} = \exp\{j\varepsilon_n(i_{\text{dop}})\} \cdot u_{\text{calc}}(k, i_{\text{dop}})_{n,n'} \cdot \exp\{-j\varepsilon_{n'}(i_{\text{dop}})\}. \tag{13}$$

Note that the phase errors are assumed to depend on element index but *not* on range. The likelihood function is given by

$$\ln\{p(i_{\text{dop}})\} = -\sum_{k=1}^{K} \{\mathbf{z}(k, i_{\text{dop}})^H \tilde{\mathbf{U}}_{\text{calc}}(k, i_{\text{dop}})^{-1} \mathbf{z}(k, i_{\text{dop}}) + \ln|\tilde{\mathbf{U}}_{\text{calc}}(k, i_{\text{dop}})|\}. \tag{14}$$

Here, $\mathbf{z}(k, i_{\text{dop}})$ is the spatial data vector obtained by extracting the N complex amplitudes from the center adjacent filter of the reduced DOF data vector in range cell k and Doppler filter i_{dop}, and K is the number of range gates in the estimation training window.

In order to estimate the phase errors, a prior distribution on the ε_n terms is added, and the derivative of the likelihood

function with respect to the phase error terms is set to zero:

$$\frac{\partial}{\partial \varepsilon_n(i_{\text{dop}})}\left\{\ln\{p(i_{\text{dop}})\} - \frac{|\varepsilon_n(i_{\text{dop}})|^2}{{\sigma_\varepsilon}^2}\right\} = 0. \tag{15}$$

The above equation is then linearized in $\varepsilon_n(i_{\text{dop}})$, and a set of linear equations is obtained. Note that a separate set of equations is solved for each Doppler filter i_{dop}.

Amplitude errors $a_n(i_{\text{dop}})$ are estimated in a similar manner. Their effect on the spatial covariance elements is modeled as

$$\begin{aligned}\tilde{\tilde{u}}_{\text{calc}}(k, i_{\text{dop}})_{n,n'} &= \exp\{a_n(i_{\text{dop}})\} \cdot \tilde{u}_{\text{calc}}(k, i_{\text{dop}})_{n,n'} \cdot \exp\{a_{n'}(i_{\text{dop}})\},\end{aligned} \tag{16}$$

where the double tilde shows that we are operating on the spatial covariance *after* phase error correction. Maximum likelihood estimation with a prior distribution, followed by linearization, is again employed.

Complex correction coefficients are defined in terms of the gain and phase corrections as

$$c_n(i_{\text{dop}}) = \exp[a_n(i_{\text{dop}}) + j \cdot \varepsilon_n(i_{\text{dop}})]. \tag{17}$$

The post-Doppler calculated covariance matrices in a given Doppler filter are then corrected using

$$\begin{aligned}&r_{\text{calc}}(k, i_{\text{dop}})_{n+(f-1)\cdot N, n'+(f'-1)\cdot N} \\ &\quad\longrightarrow c_n(i_{\text{dop}}) \cdot r_{\text{calc}}(k, i_{\text{dop}})_{n+(f-1)\cdot N, n'+(f'-1)\cdot N} \cdot c_{n'}(i_{\text{dop}})^*.\end{aligned} \tag{18}$$

Note that we assume that the phase and amplitude errors do not affect the cross covariance among adjacent Doppler filters. This assumption is of course not exactly true, since the actual errors do depend on azimuth and hence Doppler frequency.

2.3.4. Knowledge-aided prewhitening

Even after performing the adaptive gain/phase corrections described above, due to such effects as unknown internal clutter motion, residual antenna element mismatch, and aspect-dependent reflectivity, there will be errors in the clutter covariance matrices calculated from the reflectivity map. In order to combine the calculated covariance matrices with current-CPI training data, we apply an algorithm that was presented by Bergin [7] at the 2003 Adaptive Array Sensor Processing (ASAP) Conference. This algorithm fuses a calculated covariance matrix with an estimated covariance to calculate a robust STAP weight vector. The STAP weight vector is given by

$$\mathbf{w} = \kappa \cdot {\mathbf{R}_{\text{CL}}}^{-1}\mathbf{s}, \quad \mathbf{R}_{\text{CL}} \equiv \mathbf{R}_{\text{curr}} + \beta_l \cdot \mathbf{I} + \beta_d \cdot \mathbf{R}_{\text{calc}}. \tag{19}$$

This procedure is also known as "colored loading." Here $\mathbf{R}_{\text{curr}}$ is the conventional or sample covariance estimate derived from the current-CPI data cube, using the Reed-Mallett-Brennan result [4]. A range training window equal to 5 times the number of DOFs (180 range gates, corresponding to a 2.7 km range extent for the KASSPER Data Set) was used to calculate $\mathbf{R}_{\text{curr}}$. $\mathbf{R}_{\text{calc}}$ is the covariance matrix calculated from the reflectivity map (after applying the corrections described in last sub-section), $\mathbf{s}$ is the target steering vector, β_l is the conventional diagonal loading scale factor, and β_d is a "colored loading" scale factor.

It was also shown in [7] that the above STAP weight vector could be implemented using a prewhitening approach. In this approach, the data vector and the diagonally loaded range-averaged covariance estimate are prewhitened using the calculated covariance matrix. To obtain the results shown in the next section, the diagonal scale factor β_l was selected to produce diagonal loading at the noise floor. The colored loading scale factor β_d was selected so that the mean power of the $\beta_d \cdot \mathbf{R}_{\text{calc}}$ term matched that of the measured covariance $\mathbf{R}_{\text{curr}}$. Note that all quantities (matrices and vectors) are defined in the reduced post-Doppler DOF space described in Section 2.3.2.

2.3.5. Eigenvalue rescaling

To produce further improvements in residual clutter amplitude and SINR, an eigenvalue scaling technique was formulated. It involves first finding the eigenvectors and eigenvalues of the colored loading covariance:

$$\mathbf{R}_{\text{CL}}\hat{\mathbf{e}}_n = \lambda_n \hat{\mathbf{e}}_n. \tag{20}$$

A new set of eigenvalues and a modified covariance is then computed using

$$\tilde{\lambda}_n = {\hat{\mathbf{e}}_n}^H \mathbf{R}_{\text{calc}} \hat{\mathbf{e}}_n, \qquad \tilde{\mathbf{R}}_{\text{CL}} = \sum_n \tilde{\lambda}_n \cdot \hat{\mathbf{e}}_n {\hat{\mathbf{e}}_n}^H. \tag{21}$$

The final KASTAP weight vector is then computed using

$$\tilde{\mathbf{w}} = \kappa \cdot {\tilde{\mathbf{R}}_{\text{CL}}}^{-1}\mathbf{s}. \tag{22}$$

The rationale for eigenvalue rescaling is as follows. There are two important sources of error in the KASTAP covariance estimate: errors in the assumed clutter return amplitude and errors in the assumed space-time response across the antenna channels. We expect the normalized eigenvectors of the covariance matrix to be insensitive to errors in clutter return amplitude: an overall scaling of the clutter reflectivity in a given range gate will not affect the eigenvectors of the clutter covariance matrix. An amplitude scaling will, however, have a direct effect on the eigenvalues of the covariance matrix. Conversely, errors in the assumed space-time response are expected to have a large effect on the eigenvectors but little effect on the eigenvalues.

Now, we have seen (Figure 3) that the calculated covariance derived from the clutter reflectivity map produces a much better prediction of the spatial variation of clutter amplitude than the range-averaged sample covariance matrix. Since the colored loading covariance is a linear combination of the range-averaged sample covariance and the covariance

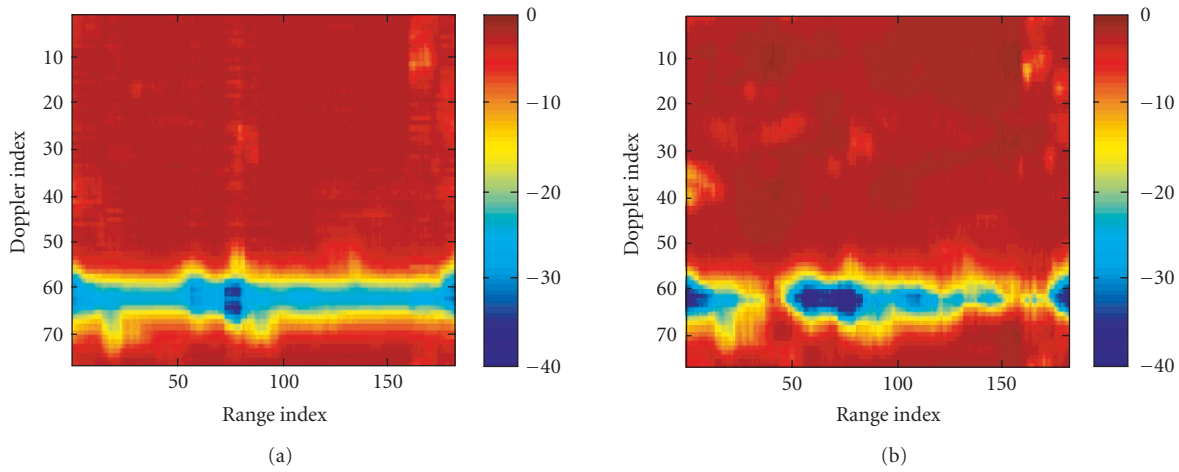

FIGURE 4: (a) SINR loss as a function of Doppler filter (vertical) and range gate (horizontal) for standard STAP processing and (b) KASTAP processing without gain/phase corrections or eigenvalue rescaling.

calculated from the clutter reflectivity map, we also expect the calculated covariance to provide a better prediction of clutter amplitude, or eigenvalues of the clutter covariance, than the colored loading covariance.

On the other hand, we have observed improvement in SINR loss using the colored loading covariance. This suggests that the space-time responses of clutter scatterers, and by implication, the clutter covariance eigenvectors, are better described by the colored loading covariance matrix. This is not so hard to believe if we realize that estimates of the space-time response are not degraded by range-averaging the way that estimates of clutter amplitude are. The space-time response of clutter at a given azimuth angle or Doppler frequency is expected to be nearly independent of range, even if the clutter amplitude is changing with range. By rescaling the eigenvalues of the colored loading covariance in the manner shown above, we are incorporating into the knowledge-aided covariance estimate improved knowledge of clutter amplitude variations provided by the clutter reflectivity map. Moreover, because we do not change the eigenvectors, we maintain the improved knowledge of clutter space-time response provided by the colored loading covariance.

3. RESULTS OF PROCESSING THE KASSPER DATA SET 2

3.1. SINR loss

Performance was first evaluated by calculating SINR loss for CPI #22 of the KASSPER Data Set 2. Figure 4 compares the SINR loss for standard STAP processing versus knowledge-aided STAP processing using the algorithm described in Section 2 without the gain/phase correction and eigenvalue rescaling steps. The loss is shown as a function of Doppler index (vertical) and range gate (horizontal) over the same region as in Figure 3. To obtain the results shown in Figure 4, data cubes without targets were processed in order to isolate the benefits on clutter suppression produced by the past CPI reflectivity map. Note from the plots that the SINR loss is degraded over a significant portion of the Doppler interval. This portion corresponds to the Doppler frequency of clutter over the antenna beamwidth. The region in which SINR loss is degraded can be compared to the areas of strong clutter return in Figure 3. Note that with knowledge-aided processing the "clutter null" is significantly narrower in certain areas. This is due to improved knowledge of the local clutter statistics that is gained from the clutter reflectivity map. Note however that the middle of the clutter null is actually deeper with KASTAP than with standard STAP processing.

Figure 5 shows the phase and log-amplitude errors as a function of Doppler filter and antenna channel that were calculated using the procedure described in the last section. Figure 6 shows the effects of incorporating these corrections on the residual clutter-to-noise ratio (CNR) after KASTAP processing. This result shows that performing the adaptive gain/phase correction significantly reduces the amount of undernulled clutter, which in turn should reduce false alarms and improve detection performance. Figure 7 shows that performing eigenvalue rescaling further reduces the residual CNR after KASTAP processing.

Figure 8 compares the SINR loss for standard STAP processing with that of KASTAP processing using multiple CPI reflectivity maps with adaptive gain and phase corrections, knowledge-aided prewhitening, and eigenvalue rescaling. Note that the middle of the clutter null after KASTAP processing is much shallower than was seen in Figure 4. This is a consequence of the reduced residual clutter levels produced by performing the adaptive gain and phase correction and eigenvalue rescaling steps. In addition, the width of the clutter null is noticeably narrower in spots than was seen in the right half of Figure 4. This is a consequence of the improved knowledge of clutter amplitude produced by performing the eigenvalue rescaling prior to STAP weight calculation. This narrowing should produce better detection of low velocity targets, which are located close to the clutter null in Doppler frequency.

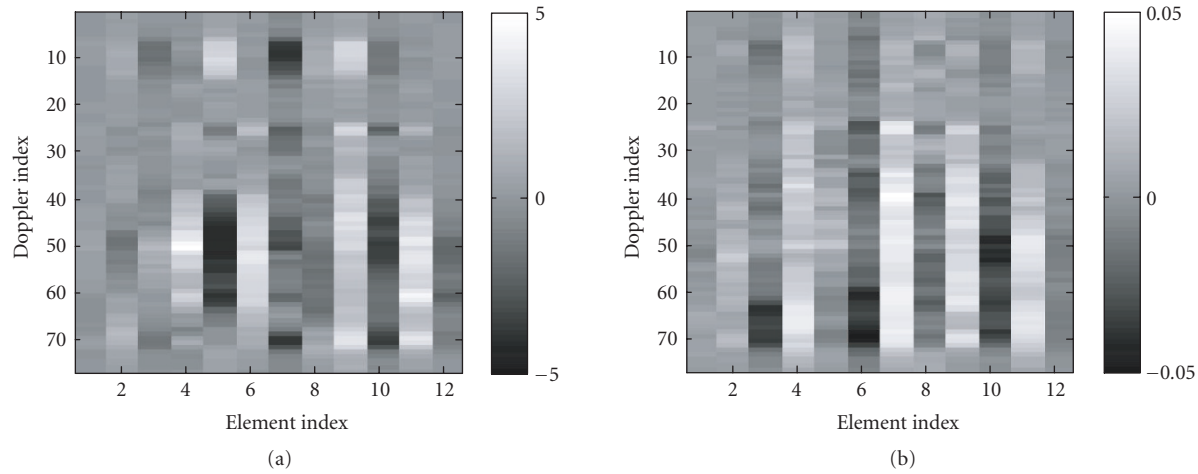

Figure 5: (a) Estimated phase and (b) long-amplitude errors as a function of Doppler filter (vertical) and antenna channel (horizontal).

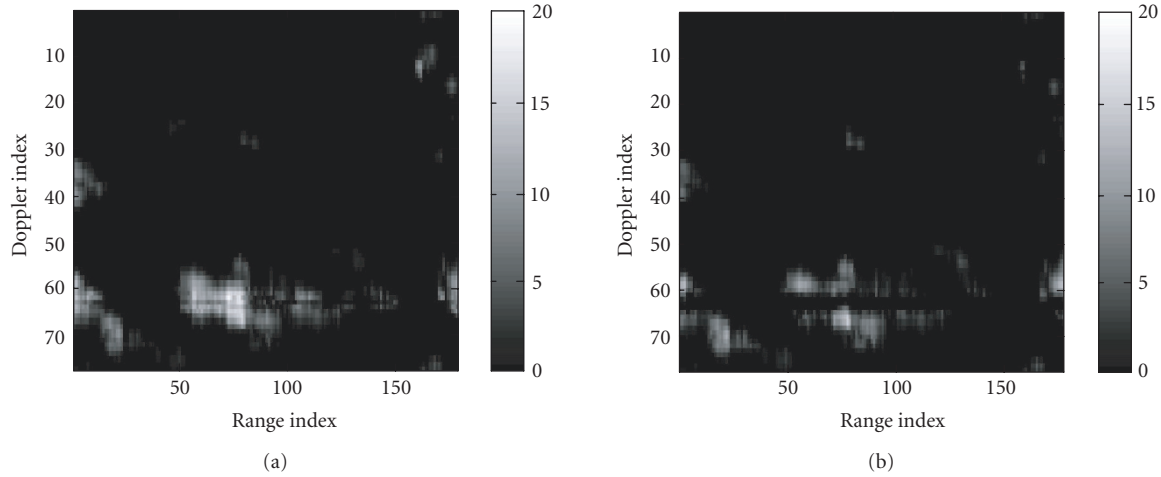

Figure 6: Residual CNR after KASTAP processing (a) without and (b) with corrections for channel- and Doppler-dependent gain and phase errors.

3.2. Detection/false alarm performance

In addition to SINR loss and residual CNR, performance was evaluated by processing the KASSPER data cubes with simulated targets in them and comparing threshold crossings to the known target range/Doppler locations. Strong discretes and targets contaminate the training data and can cause severe nulling of target returns, thus reducing target detection performance. This contamination of the range-averaged covariance estimates was reduced by performing separate range masking in each Doppler filter. To accomplish this, a two-step procedure was employed.

(1) Calculate the STAP detection statistic in each range/Doppler cell without any masking of the training data (the detection statistic is determined by normalizing the output amplitudes so that the mean output noise power is at 0 dB and then performing a range-only CFAR in each Doppler filter).

(2) Mask range/Doppler cells whose statistic exceeds a certain threshold (15 dB) from the training data. Recompute the detection statistic using the remaining training data and determine the resulting threshold crossings.

Figures 9, 10, and 11 compare the range/Doppler locations of threshold crossings in the same portion of CPI #22 as in Figures 4–8. The locations of known targets are shown as diamonds for mainlobe targets and squares for sidelobe targets. Threshold crossings due to targets are shown as light triangles, while false alarms are shown as light crosses. Observe that KASTAP produces fewer false alarms and more targets detections than standard STAP processing, especially when the adaptive gain/phase corrections and eigenvalue rescaling are performed (Figure 11).

Receiver operating characteristic (ROC) curves were generated by varying the detection threshold and counting the number of target detections and false alarms for each threshold. Probability of detection was computed by calculating the

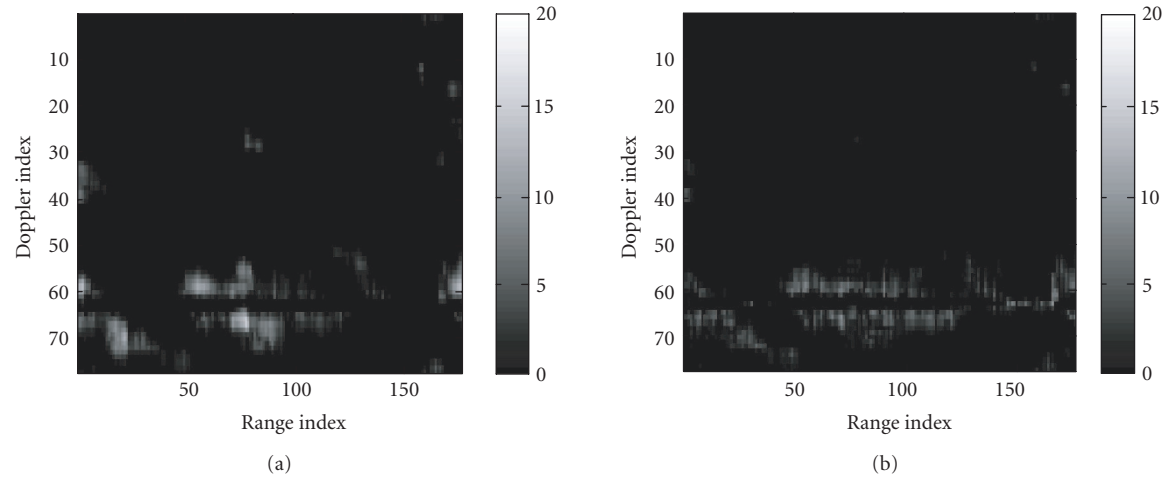

FIGURE 7: Residual CNR and KASTAP processing (with gain/phase correction) (a) without and (b) with eigenvalue rescaling.

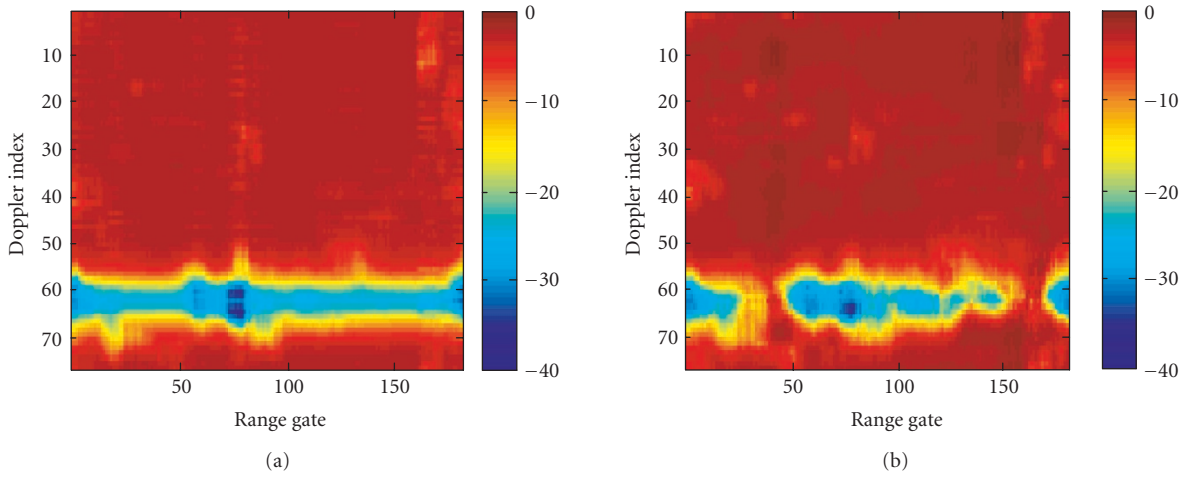

FIGURE 8: (a) SINR loss as a function of Doppler filter and range gate for standard STAP processing and (b) KASTAP processing with gain/phase correction and eigenvalue rescaling applied.

fraction of mainlobe targets that were detected within the range window processed. Multiple targets lying within the same range/Doppler cell were counted as a single target. For each threshold setting, the detection probability and false alarm density (number of alarms per square kilometer on the ground) were calculated. The range and azimuth extent processed corresponded to an area on the ground of 3 square kilometers per CPI.

Figure 12 shows the ROC curves representing performance over 29 CPIs of the KASSPER Data Set 2. A significant number of closely spaced, nonmoving targets were actually present in the scenes. Since these targets are not moving, their returns cannot be distinguished from those of clutter using Doppler frequency. Thus, even with KASTAP processing we cannot expect to achieve 100% detection probability. A consistent benefit in detection performance is seen from KASTAP processing. For example, at a detection probability of 60%, the false alarm density decreases from about 55 alarms per square kilometer for standard STAP processing to 1.5 per square kilometer for KASTAP processing (with corrections and eigenvalue rescaling), a factor of more than 30 reduction. If the nonmovers were removed from the data set, the detection probability values obtained would be expected to increase accordingly.

The effect of incorporating multi-CPI clutter reflectivity maps into knowledge-aided STAP processing on tracking performance was also evaluated using our multiple hypothesis tracking (MHT) testbed. The KASSPER Data Set 2 was again used; however only four of the targets from the data set were present in the scenario. Figure 13 shows the location of the targets on the testbed display and lists the tracking results over 23 dwells (220 seconds). For target #3, with KASTAP two tracks were actually formed. This was due to the fact that target #4 was very close to target #3, and the improved detection produced by KASTAP caused the track on target #3 to skip to target #4 near the end of the dwell sequence. The results show that with KASTAP processing, better detection performance was observed, the tracker was able to give improved time in track, and fewer false alarms were present than for standard STAP processing.

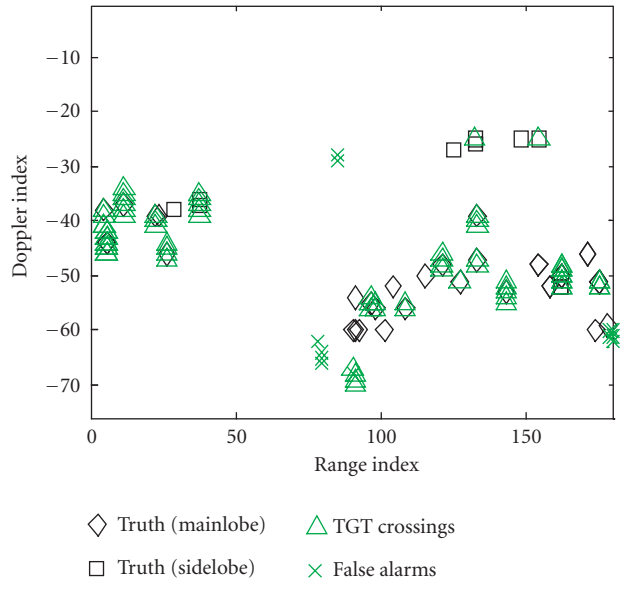

Figure 9: Range-Doppler locations of target truth (mainlobe and sidelobe targets), target threshold crossings, and false alarms for standard STAP processing on CPI #22 of the KASSPER Data Set 2.

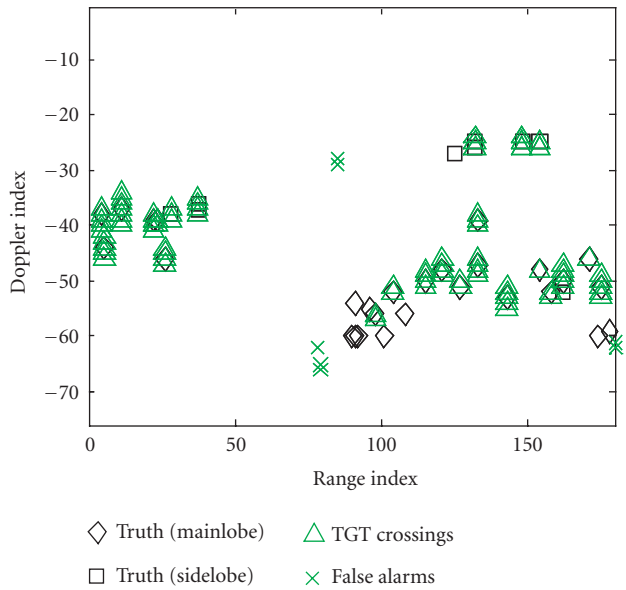

Figure 10: Range-Doppler locations of target truth (mainlobe sidelobe targets), target threshold crossings, and false alarms for KASTAP processing (without gain/phase correction or eigenvalue rescaling) on CPI #22 of the KASSPER Data Set 2.

4. MITIGATION OF LARGE DISCRETE RETURNS

The KASTAP techniques described in Sections 2 and 3 were developed for a radar interference environment consisting of strong, nonhomogeneous distributed clutter returns as well as numerous target returns. Real-world GMTI surveillance

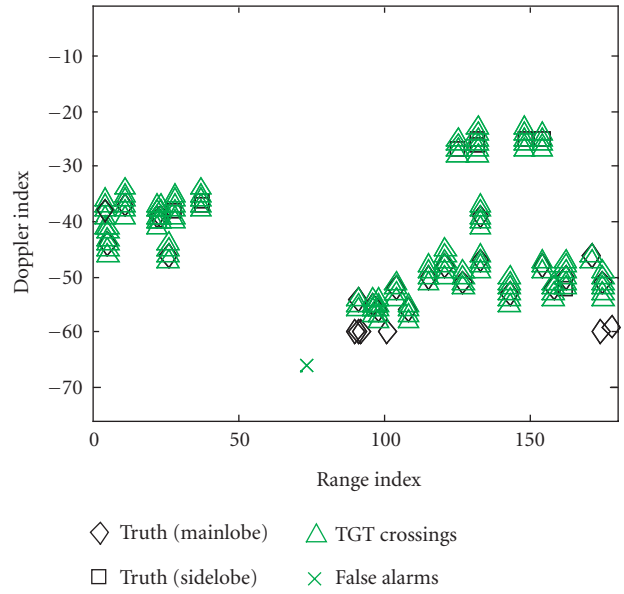

Figure 11: Range-Doppler locations of target truth (mainlobe and sidelobe targets), target threshold crossings, and false alarms for KASTAP processing (with gain/phase correction and eigenvalue rescaling) on CPI #22 of the KASSPER Data Set 2.

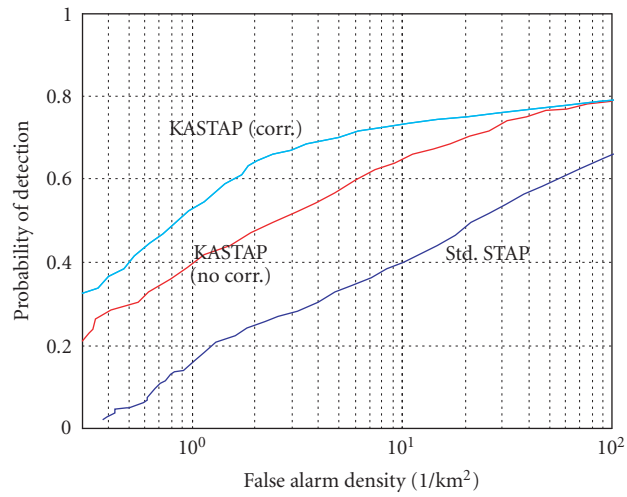

Figure 12: ROC curves for standard STAP, KASTAP without corrections or eigenvalue rescaling, and KASTAP with corrections and eigenvalue rescaling over 29 CPIs of the KASSPER Data Set 2.

conditions will also include urban areas. Such areas contain large buildings, which can produce extremely large radar returns. These returns will be much more localized than the distributed clutter returns, and are very sensitive to aspect angle. As such, they may be present on only a single CPI data cube. When they occur, the large amplitude may cause numerous false alarms to be produced in many Doppler filters. The KASTAP approach we have outlined thus far may not be sufficient to mitigate the effects of such discretes. In Section 4.1, we first show results indicating the effect of large discretes on KASTAP performance. In Section 4.2, we

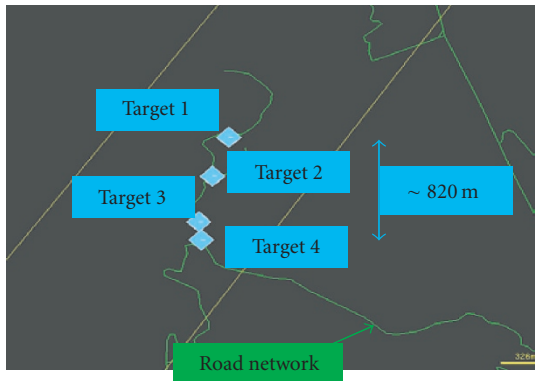

(a)

	Standard STAP	KASTAP
Target#1 detections	12	22
Target#1 time in track	130 s	230 s
Target#2 detections	17	19
Target#2 time in track	230 s	230 s
Target#3 detections	17	21
Target#3 time in track	220 s	210.20 s*
Target#4 detections	7	17
Target#4 time in track	60 s	210 s
False alarms	28	10

* Two tracks formed on target

(b)

Figure 13: (a) Target locations on our DM++ display and (b) tracking results for standard-versus-KASTAP processing.

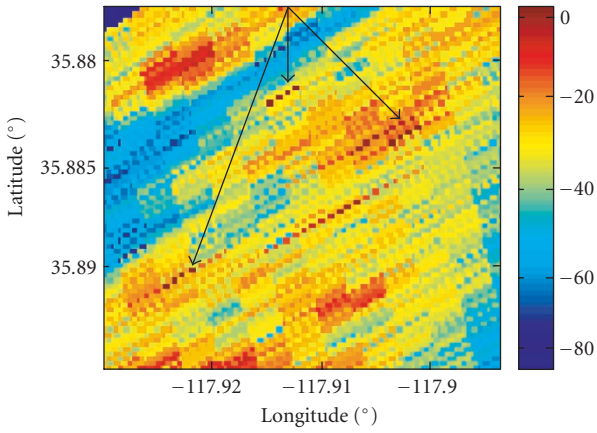

(a)

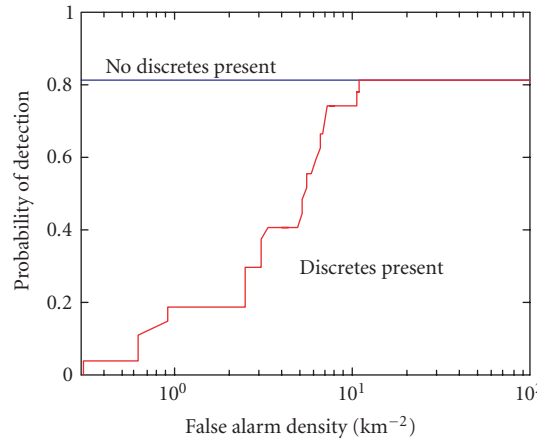

(b)

Figure 14: (a) Effects of multiple discretes on CPI #22 clutter reflectivity estimates and (b) KASTAP ROC curves.

describe a set of techniques that we developed and incorporated into our KASTAP processing to mitigate the effects of large clutter discretes. Finally, in Section 4.3 we show the results of applying these techniques to the KASSPER Data Set 2.

4.1. Effect of large discretes on KASTAP performance

Though discrete returns from buildings and towers were simulated in the KASSPER Data Set 2, the radar cross section (RCS) of these scatterers was limited by a fairly small building size [9]. In urban regions, buildings can have an RCS as high as 10^6 m^2 [12]. In order to simulate the effects of multiple large discretes, we used the routines supplied with the KASSPER Data Set 2 [9] to add plane wave responses from 5 point scatterers located on visible terrain to the CPI #22 data cube. We set the radar cross section of the discretes to be 40 dB m^2 to represent the returns from moderately large buildings.

Figure 14(a) shows that the effects of these discretes are clearly visible in the clutter reflectivity map estimates. Due to the fact that the discretes are not exactly located on one of the point scattering locations in our distributed clutter model, they corrupt reflectivity estimates over a wide area through sidelobe effects. The covariance matrices derived from the clutter reflectivity map also rely on a point scattering model. In addition, the model errors estimated for distributed clutter may be inadequate for suppressing the discrete. Thus, while there will be some suppression of the discretes by the KASTAP filter weights, undernulling can be expected to occur. With KASTAP processing, the discretes are found to produce false alarms in many Doppler filters. Figure 14(b) shows that the KASTAP ROC curves for CPI #22 are highly degraded by the presence of the discretes.

4.2. Suppression of discrete returns

We studied a number of different approaches for suppressing the effects of discretes on STAP performance. The technique we found to be most effective for suppressing the discrete returns comprises of 5 steps.

(1) Perform a thresholding of estimated clutter reflectivities in each range gate during formation of the clutter reflectivity map.

(2) Estimate the complex amplitude and azimuth angle of a discrete in each range gate containing threshold crossings from Step 1.

(3) Subtract the estimated discrete contributions to clutter reflectivity estimates.

(4) Estimate channel-dependent gain and phase errors to apply to the space-time steering vectors at the discrete locations using a maximum likelihood approach.

(5) Add an additional constraint on the STAP weight vector to place a deterministic null on each discrete.

We describe each of these steps individually below.

Step 1 (discrete detection). In this step, we detect the presence of discretes on a given CPI using the clutter reflectivity estimates. These estimates are first computed as described in Section 2.1.3. As discussed there, space-time steering vectors $\mathbf{s}_i$ to the clutter scatterers i in each range gate of a CPI data cube are first defined. The complex return strengths α_i are then calculated as shown in (5). The thresholding process in a given range gate of a CPI data cube is then specified by

$$\max_i \left\{ |\alpha_i|^2 \right\} > T. \tag{23}$$

If the threshold is crossed, we proceed to Step 2 which estimates the complex amplitude and azimuth angle of the discrete. In addition, we exclude range gates in which discretes are detected from the training data for the estimation of the distributed clutter gain and phase errors described in Section 2.3.3. This prevents the discretes from contaminating the model error terms applied to distributed clutter.

Step 2 (discrete azimuth and amplitude estimation). In this step, to prepare for removing the effects of the discrete detected in Step 1, we perform a fine estimation of the discrete azimuth angle and its complex amplitude. A bank of space-time steering vectors $\mathbf{s}_{i,j}$ is defined corresponding to a fine azimuth spacing along the clutter ridge. Here, i labels the clutter cell as in Step 1, and j is an oversample index specifying the azimuth angle within the clutter cell. We then determine the indices that maximize the following quantity:

$$\{i_d, j_d\} : \max_{\{i,j\}} |\mathbf{s}_{i,j}{}^H \mathbf{x}| = |\mathbf{s}_{i_d,j_d}{}^H \mathbf{x}|. \tag{24}$$

These indices define a maximum likelihood estimate of the discrete azimuth angle, assuming that the data vector contains only a single discrete return and additive noise. This assumption is based on the largeness of the discrete amplitude compared to distributed clutter returns. Under this model, the maximum likelihood estimate of the complex amplitude of the discrete is given by

$$\alpha_d = \frac{\mathbf{s}_{i_d,j_d}{}^H \mathbf{x}}{\mathbf{s}_{i_d,j_d}{}^H \mathbf{s}_{i_d,j_d}}. \tag{25}$$

Step 3 (clutter reflectivity map correction). In order to eliminate contamination of the clutter reflectivity estimates, during estimation of clutter reflectivity we modify the radar data vector as follows:

$$\mathbf{x} \longrightarrow \mathbf{x} - \alpha_d \cdot \mathbf{s}_{i_d,j_d}. \tag{26}$$

The complex amplitudes of each clutter scatterer are then re-estimated using (5). This effectively removes the contribution of the discrete to the clutter reflectivity map. Rather than being incorporated into the knowledge-aided covariance, a deterministic nulling of the discrete will be performed as described in Step 5.

Step 4 (discrete channel-dependent gain/phase error estimation). Though estimation of channel-dependent gain and phase errors in each Doppler filter is already being performed in our KASTAP processing, these terms will be incorrect when applied to the return from the discrete. This is due to the fact that the location of the strongest distributed clutter in each Doppler filter is different from the location of the discrete (due to the largeness of the discrete, it affects all Doppler filters through sidelobe effects). Thus, the channel- and angle-dependent antenna errors on the discrete will be different from that on distributed clutter. If we are in the Doppler filter in which the strongest distributed clutter is coming from the clutter cell containing the discrete, the differences will be much smaller. However, they will still be present and due to the strength of the discrete return, more accurate knowledge of the gain and phase errors at the discrete location is required to provide sufficient nulling.

To perform this step it was found beneficial to first perform KASTAP processing and obtain a KASTAP covariance estimate $\widetilde{\mathbf{R}}_{\mathrm{CL}}$ using the KASTAP approach we have described in previous sections. This estimate is calculated for the Doppler filter containing the maximum amplitude from the discrete (determined by applying Doppler filter weights to $\mathbf{s}_{i_d,j_d}$ and looking for the filter with the maximum amplitude). It describes the statistics of the distributed clutter returns in the range gate and Doppler filter containing the discrete. The adjacent-bin Doppler preprocessing matrix for this filter is then applied to the full-DOF data vector $\mathbf{x}$ and the discrete steering vector $\mathbf{s}_{i_d,j_d}$, yielding a reduced-DOF data vector $\mathbf{y}$ and a reduced-DOF discrete steering vector $\mathbf{s}_d$, respectively.

A set of $\mathbf{N}$ complex errors e_n, $n = 1, 2, \ldots, N$, is next defined. These error terms define a modified, reduced-DOF discrete space-time steering vector whose elements are given by

$$\left[s_d^{(\mathrm{corr.})} \right]_{n+(f-1)\cdot N} = (1 + e_n) \cdot [s_d]_{n+(f-1)\cdot N}. \tag{27}$$

Here, n is the antenna channel index and f is the adjacent filter index for the adjacent-bin post-Doppler degrees algorithm. To determine the error terms, we model the reduced-DOF data vector $\mathbf{y}$ in the range gate containing the discrete as

$$\mathbf{y} = \alpha_d \cdot \mathbf{s}_d^{(\mathrm{corr.})} + \mathbf{y}_c, \tag{28}$$

where $\mathbf{y}_c$ is a complex Gaussian random vector with covariance matrix $\widetilde{\mathbf{R}}_{\mathrm{CL}}$ (representing the distributed clutter). The complex error terms e_n, $n = 1, 2, \ldots, N$, are next selected to

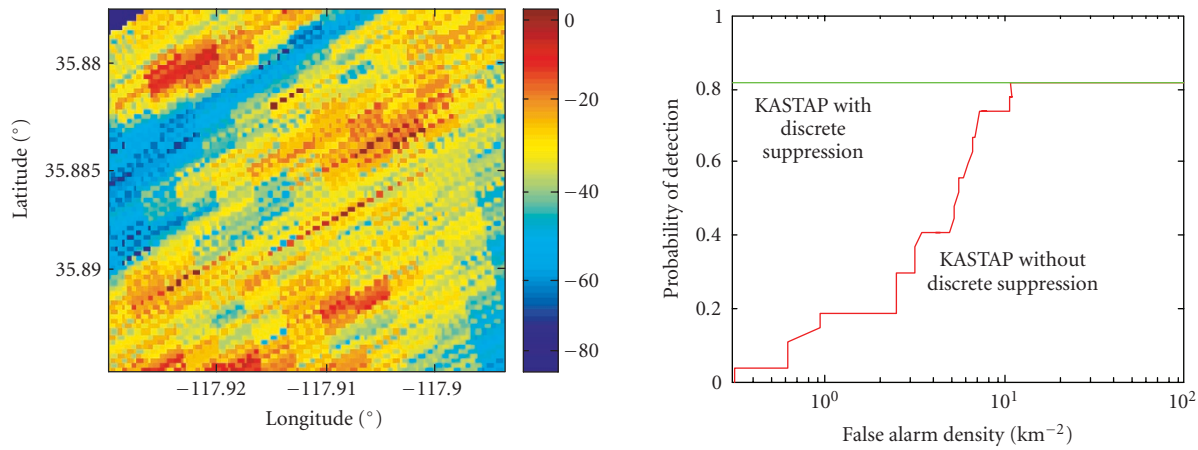

(a) (b)

FIGURE 15: (a) Effects of discrete suppression processing on CPI #22 clutter reflectivity estimates and (b) KASTAP ROC curves.

maximize the log-likelihood function

$$\ln p(\mathbf{y} \mid e) = -\left(\mathbf{y} - \alpha_d \cdot \mathbf{s}_d^{(\text{corr.})}\right)^H \widetilde{\mathbf{R}}_{\text{CL}}{}^{-1} \left(\mathbf{y} - \alpha_d \cdot \mathbf{s}_d^{(\text{corr.})}\right) - \sum_{n=1}^{N} \frac{|e_n|^2}{\sigma_e{}^2} + \text{const}. \tag{29}$$

Note that we have added a complex Gaussian prior distribution on e_n with variance $\sigma_e{}^2$. The variance is selected to be $\ll 1$ in order to force the constraint that the errors are small. We next vary the log-likelihood function with respect to the real and imaginary parts of e_n (or, equivalently, with respect to e_n and $e_n{}^*$). Remembering that $\mathbf{s}_d^{(\text{corr.})}$ depends on e_n as shown above, equating the coefficients of δe and δe^* to zero gives a linear set of equations for the error terms e_n which are readily solved.

Note that we have used a particular Doppler filter, the filter with the largest discrete amplitude contribution, to estimate the channel-dependent gain error terms on the discrete. In Step 5 we want to use this information to improve STAP performance in *all* the Doppler filters. In order to do this, once the error terms are obtained, the corrected *full-DOF* space-time steering vector for the discrete is calculated as

$$\left[s_{i_d,j_d}^{(\text{corr.})}\right]_{n+(m-1)\cdot N} = (1 + e_n) \cdot \left[s_{i_d,j_d}\right]_{n+(m-1)\cdot N}. \tag{30}$$

(Here, m is the pulse index ranging from 1 to the number of pulses M.) In Step 5, we compute corrected reduced-DOF discrete steering vectors in *each* Doppler filter by applying the appropriate Doppler preprocessing matrix to the corrected full-DOF steering vector shown above.

Step 5 (KASTAP filter weights with deterministic null on discrete). Given an estimated covariance $\widetilde{\mathbf{R}}_{\text{CL}}$, the "standard" KASTAP weight vector $\mathbf{w}_{\text{KA}}$ is computed by minimizing $\mathbf{w}_{\text{KA}}{}^H \widetilde{\mathbf{R}}_{\text{CL}} \mathbf{w}_{\text{KA}}$ subject to a gain constraint on the target steering vector $\mathbf{s}_t$. This gives the familiar expression

$$\mathbf{w}_{\text{KA}} = \beta \cdot \widetilde{\mathbf{R}}_{\text{CL}}{}^{-1} \mathbf{s}_t. \tag{31}$$

We modified this to apply, in addition to the target gain constraint, a null constraint on the corrected, reduced-DOF discrete steering vector. This is repeated in *each* Doppler filter, not just the filter containing the maximum discrete amplitude, so that the sidelobe effects of the discrete can also be removed. In a given Doppler filter q, we define a corrected reduced-DOF steering vector $\mathbf{s}_d^{(q,\text{corr.})}$ by applying the adjacent-bin preprocessing matrix for filter q to the vector $\mathbf{s}_{i_d,j_d}^{(\text{corr.})}$ shown in (30).

Next, we solve the constrained minimization problem

$$\min_{\mathbf{w}_{\text{KA}}} \mathbf{w}_{\text{KA}}{}^H \widetilde{\mathbf{R}}_{\text{CL}} \mathbf{w}_{\text{KA}} \quad \text{s.t. } \mathbf{w}_{\text{KA}}{}^H \mathbf{s}_t = 1,\ \mathbf{w}_{\text{KA}}{}^H \mathbf{s}_d^{(q,\text{corr.})} = 0. \tag{32}$$

This can be solved using Lagrange multipliers, yielding

$$\mathbf{w}_{\text{KA}} = \beta \cdot \widetilde{\mathbf{R}}_{\text{CL}}{}^{-1} \left(\mathbf{s}_t - \gamma \cdot \mathbf{s}_d^{(q,\text{corr.})}\right), \qquad \gamma = \frac{\mathbf{s}_d^{(q,\text{corr.})^H} \widetilde{\mathbf{R}}_{\text{CL}}{}^{-1} \mathbf{s}_t}{\mathbf{s}_d^{(q,\text{corr.})^H} \widetilde{\mathbf{R}}_{\text{CL}}{}^{-1} \mathbf{s}_d^{(q,\text{corr.})}}. \tag{33}$$

It is easily verified that this weight vector satisfies the null constraint $\mathbf{w}_{\text{KA}}{}^H \mathbf{s}_d^{(q,\text{corr.})} = 0$. The constant β is selected to satisfy the target gain constraint (however, since it is only an overall scale factor, β has no effect on the output SINR or CNR).

4.3. KASTAP results with discrete suppression processing

The 5-step approach described in the last section was applied to the 5-discrete scenario that was discussed in Section 4.1. The threshold level was set to $T = 35$ dB. Figure 15 shows the results corresponding to Figure 14 for KASTAP processing with discrete suppression added. Figure 15(a) shows that

the "cleaning" procedure (Step 3 of the procedure described in the last section) was effective in removing the large amplitude contributions of the discrete to the clutter reflectivity map. Figure 15(b) shows that all of the degradation in the ROC curve caused by the discretes has been eliminated through use of the discrete suppression algorithm described in the last section.

5. SUMMARY

We have described in this paper knowledge-aided STAP processing using multilook GMTI radar data. The algorithm registers the data to an earth-based coordinate system and forms clutter reflectivity maps, which are used to calculate predicted distributed clutter statistics. Adaptive incorporation of current-CPI data into the reflectivity maps is also performed to improve local reflectivity estimates when large changes occur as the platform geometry evolves. The clutter reflectivity map predictions are incorporated into robust STAP processing using a procedure that combines covariance tapering to account for ICM, adaptive correction for Doppler and channel-dependent gain and phase mismatch, knowledge-aided prewhitening, and eigenvalue rescaling. The effects of target contamination of the STAP training data are suppressed from the covariance estimates in each Doppler filter using masking of detections in a two-pass procedure. The approach was applied to the KASSPER Data Set 2 and KASTAP performance characterized in terms of SINR loss, residual CNR, target detections and false alarms, ROC curves, and track life. The results show improved detection of low-velocity targets and more than an order of magnitude reduction in false alarm density compared to standard STAP processing. Additional techniques to detect and suppress large clutter discretes have been defined and shown to be effective in reducing the degradation in KASTAP performance caused by these discretes.

ACKNOWLEDGMENT

The authors would like to thank the Defense Advanced Research Projects Agency for funding this work under Contract F30602-02-C-0010.

REFERENCES

[1] W. L. Melvin, "Space-time adaptive radar performance in heterogeneous clutter," *IEEE Transactions on Aerospace and Electronic Systems*, vol. 36, no. 2, pp. 621–633, 2000.

[2] W. L. Melvin, J. R. Guerci, M. J. Callahan, and M. C. Wicks, "Design of adaptive detection algorithms for surveillance radar," in *Proceedings of Record of the IEEE 2000 International Radar Conference*, pp. 608–613, Alexandria, Va, USA, May 2000.

[3] J. Ward, "Space-time adaptive processing for airborne radar," Tech. Rep. F19628-95-C-0002, MIT Lincoln Laboratory, Lexington, Mass, USA, 1994.

[4] I. S. Reed, J. D. Mallett, and L. E. Brennan, "Rapid convergence rate in adaptive arrays," *IEEE Transactions on Aerospace and Electronic Systems*, vol. 10, no. 6, pp. 853–863, 1974.

[5] J. R. Guerci, "Theory and application of covariance matrix tapers for robust adaptive beamforming," *IEEE Transactions on Signal Processing*, vol. 47, no. 4, pp. 977–985, 1999.

[6] R. C. DiPietro, "Extended factored space-time processing for airborne radar systems," in *Proceedings of 26th IEEE Asilomar Conference on Signals, Systems and Computers*, vol. 1, pp. 425–430, Pacific Grove, Calif, USA, October 1992.

[7] J. S. Bergin, J. R. Guerci, P. M. Techau, and C. M. Teixeira, "Space-time beamforming with knowledge-aided constraints," in *Proceedings of 11th Workshop on Adaptive Sensor Array Processing (ASAP '03)*, Lexington, Mass, USA, March 2003.

[8] J. S. Bergin, C. M. Teixeira, P. M. Techau, and J. R. Guerci, "STAP with knowledge-aided data pre-whitening," in *Proceedings of IEEE Radar Conference*, pp. 289–294, Philadelphia, Pa, USA, April 2004.

[9] "High-Fidelity Site-Specific Radar Simulation: KASSPER Data Set 2," Information Systems Laboratories, Inc., October 2002.

[10] E. J. Kelly, "An adaptive detection algorithm," *IEEE Transactions on Aerospace and Electronic Systems*, vol. 22, no. 1, pp. 115–127, 1986.

[11] L. Novak, "New results in UHF/VHF SAR change detection," in *CCC&D FOPEN Workshop*, MIT Lincoln Laboratory, Lexington, Mass, USA, October 2002.

[12] M. I. Skolnik, Ed., *Radar Handbook*, McGraw-Hill, New York, NY, USA, 2nd edition, 1990, Section 17.2.

Douglas Page received the B.S. (1983) and M.Eng. (1984) degrees in electrical engineering, and the Ph.D. (1992) degree in physics from Rensselaer Polytechnic Institute. From 1993 to 2000, he was with Technology Service Corporation (TSC) in Trumbull, Conn, working on a variety of problems in radar simulation and algorithm development. This included developing and simulating the performance of space-time adaptive processing (STAP) algorithms. From April 2000 through October 2002, Dr. Page was with the MITRE Corporation in Bedford, Mass, where he continued work in radar signal processing, including target detection in synthetic aperture radar (SAR) imagery. He joined BAE Systems in November 2002, where he has been developing STAP techniques in connection with several different programs. Dr. Page is a Member of the Tau Beta Pi, Eta Kappa Nu, and Signal Xi Honor Societies.

Gregory Owirka received the B.S. degree (1987) from Southeastern Massachusetts University in applied mathematics and the M.S. degree (1999) from the Northeastern University in electrical engineering. From 1987 to 2002, he worked at MIT Lincoln Laboratory as a Technical Staff Member, developing algorithms and performing data analysis in the area of synthetic aperture radar (SAR) detection, discrimination, and classification. Mr. Owirka worked in a team that developed the first end-to-end ATR system, specifically designed to exploit high-resolution, fully polarimetric SAR imagery. He developed many of the core algorithms for an automatic target-cueing (ATC) system, including a multistage, template-based recognition system that used super-resolved SAR imagery to enhance recognition performance. From 2002 to the present, Mr. Owirka works at BAE Systems, Advanced Information Technologies, where he is the Section Leader of the Moving Target Technologies (MTT) Section. Mr. Owirka has published extensively in the areas of airborne radar surveillance, automatic target recognition, and sensor exploitation.